Original Article

Integrating myocardial metabolic imaging and stress myocardial contrast echocardiography to improve the diagnosis of coronary microvascular diseases in rabbits

Guodong Wang[1#], Xiaohong Li[2#], Jiaxin Zhao[1], Shangke Chen[1], Yongde Qin[2], Lina Guan[1], Yuming Mu[1]

[1]Department of Echocardiography, The First Affiliated Hospital of Xinjiang Medical University, Xinjiang Key Laboratory of Ultrasound Medicine, Urumqi, China; [2]Department of Nuclear Medicine, The First Affiliated Hospital of Xinjiang Medical University, Urumqi, China

Contributions: (I) Conception and design: G Wang, X Li, Y Mu; (II) Administrative support: Y Qin, L Guan, Y Mu; (III) Provision of study materials or patients: G Wang, X Li, J Zhao, L Guan; (IV) Collection and assembly of data: G Wang, X Li, J Zhao; (V) Data analysis and interpretation: G Wang, X Li, J Zhao, S Chen, Y Mu; (VI) Manuscript writing: All authors; (VII) Final approval of manuscript: All authors.

[#]These authors contributed equally to this work.

Correspondence to: Yuming Mu, PhD. Department of Echocardiography, The First Affiliated Hospital of Xinjiang Medical University, Xinjiang Key Laboratory of Ultrasound Medicine, No, 137, Liyushan South Road, Urumqi 830000, China. Email: mym1234@126.com.

Background: Persistent challenges associated with misdiagnosis and underdiagnosis of coronary microvascular disease (CMVD) necessitate the exploration of noninvasive imaging techniques to enhance diagnostic accuracy. Therefore, we aimed to integrate multimodal imaging approaches to achieve a higher diagnostic rate for CMVD using high-quality myocardial metabolism imaging (MMI) and myocardial contrast echocardiography (MCE). This combination diagnostic strategy may help address the urgent need for improved CMVD diagnosis.

Methods: In this study, we established five distinct pretreatment groups, each consisting of nine male rabbit: a fasted group, a nonfasted group, a sugar load group, an acipimox group, and a combination group of nonfasted rabbits administered insulin. Moreover, positron emission tomography-computed tomography (PET/CT) scan windows were established at 30-, 60-, and 90-minute intervals. We developed 10 CMVD models and conducted a diagnosis of CMVD through an integrated analysis of MMI and MCE, including image acquisition and processing. For each heart segment, we calculated the standardized uptake value (SUV) based on body weight (SUV_{bw}), as well as certain ratios of SUV including SUV of the heart (SUV_{heart}) to that of the liver (SUV_{liver}) and SUV_{heart} to SUV of the lung (SUV_{lung}). Additionally, we obtained three coronary SUV_{bw} uptake values. To clarify the relationship between SUV_{bw} uptake values and echocardiographic parameters of the myocardial contrast agent more thoroughly, we conducted a comprehensive analysis across different pretreatment protocols. Receiver operating characteristic (ROC) curve analysis was employed to evaluate the diagnostic accuracy of each parameter in the context of CMVD.

Results: In the context of MMI, the nonfasted-plus-insulin group, as observed during the 60-minute examination, exhibited a noteworthy total ^{18}F-fluorodeoxyglucose (^{18}F-FDG) uptake of 47.44±6.53 g/mL, which was found to be statistically different from the other groups. To ascertain the reliability of the results, two double-blind investigators independently assessed the data and achieved a good level of agreement, according to the intraclass correlation coefficient (ICC) (0.957). The SUV_{bw} of the nonfasted-plus-insulin group exhibited a moderate correlation with the microvascular blood flow reserve (MBFR) parameters derived from the MCE examination, as evidenced by a *r* value of 0.686. For the diagnosis of CMVD disease, the diagnostic accuracy of the combined diagnostic method [area under the curve (AUC) =0.789; 95% confidence interval (CI): 0.705–0.873] was significantly higher than that of the MBFR (AUC =0.697; 95% CI: 0.597–0.797) and SUV_{bw} (AUC =0.715; 95% CI: 0.622–0.807) methods (P<0.05).

Conclusions: Our study demonstrated the feasibility of a simple premedication approach involving free feeding and intravenous insulin in producing high-quality gated heart ^{18}F-FDG PET/CT images in adult male New Zealand white rabbits. This technique holds considerable potential for ischemic heart disease research in rabbits and can enhance CMVD diagnosis via the comprehensive assessment of myocardial metabolism and perfusion.

Keywords: Coronary microvascular disease (CMVD); myocardial contrast echocardiography (MCE); positron emission tomography-computed tomography (PET/CT); ^{18}F-fluorodeoxyglucose (^{18}F-FDG); rabbit

Submitted Nov 16, 2023. Accepted for publication Jul 10, 2024. Published online Jul 30, 2024.
doi: 10.21037/qims-23-1630
View this article at: https://dx.doi.org/10.21037/qims-23-1630

Introduction

The timely identification of coronary microvascular disease (CMVD) is a crucial endeavor in disease prevention and management (1,2). Recent research in this field has primarily focused on multimodal imaging techniques (3,4), with positron emission tomography-computed tomography (PET/CT) being recognized as the gold standard for noninvasive myocardial ischemia diagnosis and providing unparalleled insights (5,6). Additionally, myocardial metabolism imaging (MMI) plays a vital role in evaluating cardiomyocyte functionality in the context of myocardial ischemia diagnosis. This approach offers an objective assessment of the extent and severity of myocardial ischemia (7). Interestingly, the impact of glucose metabolism on image fidelity is a key determinant of imaging quality. Stress myocardial contrast echocardiography (MCE) has emerged as an invaluable technique, as it can monitor and qualitatively and quantitatively assess microvascular hemodynamic parameters (8). Among these parameters, myocardial blood flow (MBF) and microvascular blood flow reserve (MBFR) fraction are of paramount importance (9). As diagnosis of CMVD is marred by a high prevalence of underdiagnosis and misdiagnosis (10), a combined diagnosis approach incorporating MMI and MME has the potential to improve diagnostic accuracy by providing a comprehensive characterization of myocardial structure, microvascular reserve function, and tissue metabolic abnormalities (7).

The quality of the PET/CT image has a significant impact on the assessment of myocardial survival outcomes when ^{18}F-fluorodeoxyglucose (^{18}F-FDG) PET/CT MMI is being performed. Fatty acids, amino acids, glucose, pyruvate, and lactate are all used as energy substrates in the metabolism of human cardiomyocytes, and insulin is the primary regulatory hormone in the use of blood glucose by cardiomyocytes. Clinical studies suggest that myocardial ^{18}F-FDG uptake can be enhanced through an approach combining glycemic load and insulin (7). However, there is a dearth of preclinical research on the quality of cardiac PET/CT imaging. In this study, we focused on metabolic and perfusion functions in CMVD. We chose rabbits for this study because their coronary system closely resembles that of humans and their large size facilitates the acquisition of high-resolution images. Although mice and rats are the most commonly used small-animal imaging models, their small size and rapid heart rate require more technically demanding and sophisticated imaging equipment to achieve similar results. Furthermore, while pigs and dogs are easier to handle and image, they are expensive and difficult to transport. With consideration to cost-effectiveness, coronary structure, the acquisition of high-resolution images, and ease of experimental manipulation, rabbits are ideal for multimodal imaging studies of CMVD. After conducting our experiments, we observed that it was not possible to achieve stable MMI using the standard preprocessing protocols. Therefore, in order to effectively obtain MMI in rabbits, it is crucial to consider their specific metabolic profile. These herbivorous animals consume diets rich in carbohydrates, proteins, and fatty acids, leading to intricate changes in gastrointestinal hormone signaling that influences processes ranging from nutrient assimilation to satiety regulation (11). The myocardial metabolism in rabbits is still a relatively underexplored subject (12), and we thus aimed to improve myocardial uptake in rabbits, obtain high-quality images, and establish a model examination protocol. This work may provide solutions to the persistent

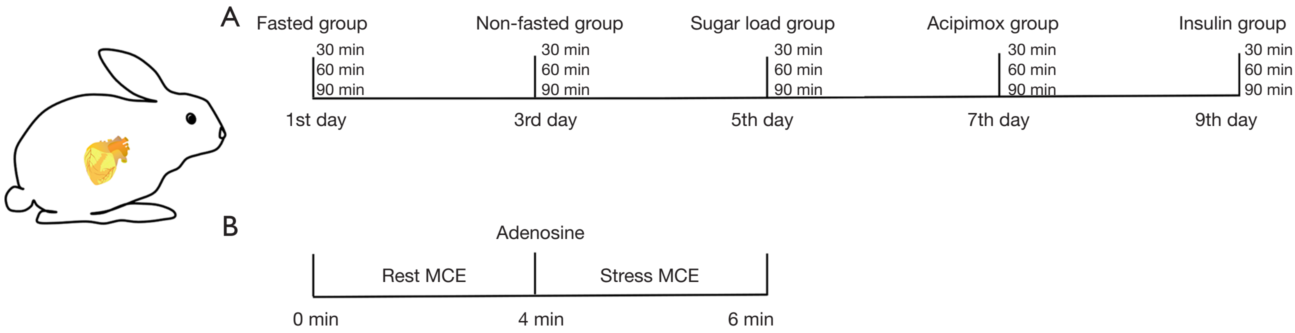

Figure 1 Experimental design, examination process, and diagram of myocardial metabolism phenomenon for the various pretreatment methods. (A) The pretreatment conditions and examination time windows of the different experimental protocols. (B) Procedure for stress MCE. MCE, myocardial contrast echocardiography.

diagnostic and therapeutic challenges in experimental cardiology.

The principal aim of this study was to diagnose CMVDs by integrating stable MMI with stress MCE. Additionally, we sought to examine the correlation between ^{18}F-FDG uptake parameters and myocardial perfusion under various pretreatment protocols. A dual-modality assessment of myocardial viability and perfusion is proposed to enhance the precision of diagnosing CMVD and lay the groundwork for accurate CMVD diagnosis using molecular imaging techniques. We present this article in accordance with the ARRIVE reporting checklist (available at https://qims.amegroups.com/article/view/10.21037/qims-23-1630/rc).

Methods

Animal model and experimental protocol

In this experiment, healthy male New Zealand white rabbits were obtained from the Animal Research Center of Xinjiang Medical University. Experiments were performed under a project license (No. IACUC-20210725-15) granted by the Experimental Animal Ethics Committee of Xinjiang Medical University and in compliance with institutional guidelines for the care and use of animals. All procedures involving animals adhered to the institutional guidelines for the care and use of laboratory animals. A protocol was prepared before the study without registration.

This study includes five pretreatment group groups and three-time windows, with nine male rabbits being required for each two-way analysis of variance (ANOVA). We used G*Power software to calculate the sample size required for two-way ANOVA.

Nine healthy male rabbits were carefully selected for the study to ensure good cardiac health and optimal function throughout echocardiography. All the New Zealand white rabbits enrolled in the study demonstrated sustained normoglycemia and systolic function throughout a continuous three-day period prior to the initiation of experimental procedures. The experiment was organized into five intervention cohorts as described below (see also *Figure 1A*):

- (I) Fasted group (n=9): rabbits in this category were fasted for 6–8 hours, with without access to food or water.
- (II) Nonfasted group (n=9): rabbits in this group had unrestricted access to food.
- (III) Sugar load group (n=9): following a fasting period of 6–8 hours, rabbits received a glucose solution at a dose of 3 g/kg. An intravenous injection of ^{18}F-FDG was administered when their blood glucose levels reached 7.9 to 8.8 mmol/L.
- (IV) Acipimox group (n=9): these rabbits were administered a gavage of 50 mg/kg of acipimox, followed by an intravenous injection of ^{18}F-FDG.
- (V) Nonfasted + insulin group (n=9): rabbits received an intravenous injection of insulin at a dose of 0.1 IU/kg via the ear margin. Blood glucose levels were closely monitored, and the injection of ^{18}F-FDG was administered when a 20% reduction in blood glucose levels was observed. Notably, blood glucose levels were measured twice before the intervention, both before and after the PET/CT examination.

The rabbits were anesthetized using a freshly prepared 0.7% sodium pentobarbital solution administered intravenously through the ear margin. PET/CT scans were carried out in all specified groups at 30, 60, and 90 minutes after the intravenous injection of ^{18}F-FDG. The rabbits were positioned in a supine posture and securely immobilized. PET/CT examinations were conducted with continuous ECG monitoring. It is essential to emphasize that a one-day interval was observed between each group of rabbits and their respective experimental sessions, as depicted in *Figure 1A*. A one-day interval was implemented between scans to allow sufficient recovery time for the animals, facilitating the metabolism of pentobarbital sodium and ^{18}F-FDG radiotracer. The Xeleris functional imaging workstation (GE HealthCare, Chicago, IL, USA) was employed to extract the standardized uptake value (SUV) based on body weight (SUV_{bw}), a pivotal metric for evaluating myocardial metabolic activity in each segment.

Time window for ^{18}F-FDG PET/CT examination

This precise quantification enabled a detailed analysis of the PET/CT examination at specific time intervals after administration. These examination intervals were established at 30, 60, and 90 minutes, aligning with the experimental group that produced the highest image quality. The purpose of selecting these specific time intervals for the PET/CT examination was to investigate the relationship between the visual quality of MMI and the timeframes following administration. This systematic analysis provided a comprehensive understanding of how the temporal window of the PET/CT examination influences the resulting quality of MMI.

^{18}F-FDG PET/CT examination parameters

A Discovery PET/CT system (GE HealthCare) was used for the PET/CT scan. A precise dose of 1 mCi/kg of ^{18}F-FDG was intravenously administered and allowed to circulate for 60 minutes before imaging. An eight-minute static scan was conducted using a gated acquisition protocol, capturing comprehensive three-dimensional images. The acquisition parameters included a 40-mm detector coverage and a 2.5-mm helical thickness, ensuring detailed imaging.

Further precision was achieved with a pitch speed of 0.984, specific values of 139.37 mm/rotation, and a rotation time of 0.5 mm. The collected scan data underwent robust reconstruction with a 35-cm diameter, 128×128 transverse matrix. The ordered subset expectation maximization algorithm, integrated into the 3D VUE software (GE HealthCare), was applied. CT attenuation correction was an integral component of the reconstruction process and used an iterative approach of four iterations and eight subsets. This comprehensive procedure resulted in essential imaging views, including left ventricular short axis, main longitudinal, and main horizontal tomographic images.

Consistency was critical to the experiment, with the same parameters being carefully maintained for each scan and subsequent reconstruction. This commitment to precision, coupled with advanced technology, yielded comprehensive and informative results.

Quantitative analysis of ^{18}F-FDG PET/CT imaging

The Xeleris functional imaging workstation was used for the precise measurement of ^{18}F-FDG uptake SUV_{bw} values in heart 17 segments, including coronal, sagittal, and axial views, to assess myocardial metabolic activity. SUV_{bw} values of liver and lung tissues were also evaluated to calculate the ratio of SUV of the heart (SUV_{heart}) to the SUV of the liver (SUV_{liver}) and that of SUV_{heart} to the SUV of the lung (SUV_{lung}), enabling a comprehensive assessment of cardiometabolic parameters. To ensure accuracy, measurements were repeated three times for each image set. Data analyses were conducted under a single-blind method with two independent observers.

MCE examination parameters

Following anesthesia, intravenous access was established via the ear vein. A specialized contrast agent (SonoVue, Bracco, Italy) was employed to enhance ultrasound imaging. MCE was conducted to evaluate myocardial perfusion both at rest and during stress using a EPIQ 7C ultrasound diagnostic instrument (Philips, Amsterdam, the Netherlands) (*Figure 1B*). The contrast mode parameters were standardized, including an image depth of 50 mm, a gain setting at 55 dB, a focal point alignment at the level of the mitral valve, a dynamic range of 50 dB, and a mechanical index (MI) of 0.18. A syringe pump (LD-P2020, Shanghai Rande Medical Instrument Co., Shanghai, China) was connected, facilitating the continuous administration of the contrast agent through the auricular venous channel at a rate of 0.5 mL/min. Dynamic short-axis images of the left ventricle were captured with a 10-second data acquisition time per dataset and saved in Digital Imaging and Communications in Medicine (DICOM) format for subsequent offline analysis. The stress MCE examination was conducted in the fourth minute, mirroring the procedures used in the resting MCE examination. Adenosine (Aiduo, Shenyang, China) was infused at a rate of 0.19 mL/min, with a dosage of 140 μg/(kg·min) over three minutes. These settings were consistently applied across all parameters.

Quantitative analysis of MCE

Microvascular perfusion was assessed using QLAB version 9.0 software (Philips). The analysis focused on defining a specific region of interest (ROI) within myocardial segments during the end-systolic phase. This excluded structures such as the left ventricular cavity and pericardium for precise examination. Through an exponential curve fitting equation, the software computed two parameters for each ROI. The plots of myocardial video (contrast) intensity and pulse interval are fit to an exponential function: $VI = A (1 - e^{-\beta t})$, where VI is the video intensity at PI t, A is the video intensity at the plateau, and β is the rate of increase of the video intensity after the destruction of the bubble. MBF is estimated by the product of A×β, where A (plateau video intensity) reflects microvascular cross-sectional area and β (video intensity rise rate) represents microbubble or MBF velocity. Measurements were repeated three times for precision. To calculate reserve function, A reserve (A_{stress}/A_{rest}) and β reserve ($\beta_{stress}/\beta_{rest}$) were determined, as was local myocardial microvascular reserve function (MBF reserve: MBF_{stress}/MBF_{rest}). This advanced method allowed for precise microvascular perfusion analysis, providing insights into the cardiac dynamics during the end-systolic phase.

Our study focused on correlation analyses and specifically examined the relationships between the A, β, MBF, MBFR, and SUV_{bw} measurements.

Construction of a rabbit model of coronary microvascular dysfunction

In a cohort of 10 healthy male New Zealand large white rabbits, the right common carotid artery was surgically isolated. With the aid of a diagnostic ultrasound device (Philips EPIQ 7C), we carefully tracked the position of the balloon catheter and monitored its echoes within the ascending aorta. Under the guidance of ultrasound, a 28-gauge fine needle was precisely inserted into the left ventricle in alignment with the ultrasound beam. Subsequently, the balloon catheter was infused with saline to temporarily halt blood flow in the ascending aorta for approximately 20 seconds. A solution of sodium lauryl sulfate (dosage: 2.8 mg/kg; concentration: 40 mg/mL) was promptly injected into the left ventricular cavity, followed by the rapid deflation of the balloon. Throughout the procedure, vital signs were continuously monitored, and sutures were tightly secured to complete the surgical intervention.

On the third postoperative day, sequential ^{18}F-FDG PET/CT imaging and MCE were conducted under the same parameters and protocols as those used in the previous procedures. Following the examination, myocardial specimens were collected and preserved for histopathological hematoxylin and eosin (HE) staining analysis and for immunofluorescence staining of CD31.

HE and immunofluorescence

HE staining was used to identify pathologic changes, and immunofluorescent staining was used to identify vascular endothelial cells (CD31) in frozen sections of cardiac tissue. CD31 antibody (GTX20218, GeneTex, Irvine, CA, USA) was diluted at 1:500 in phosphate-buffered saline and allowed to incubate at room temperature for two hours. The secondary antibody (CY5; ab52061, Abcam, Cambridge, UK) was then added to the samples at a 1:1,000 dilution in phosphate-buffered saline for 50 minutes in the dark at 37 ℃. This was followed by the application of a solution of 4’6-diamidino-2-phenylindole for 10 minutes for nuclear staining. After the samples were mounted, the slides were processed and evaluated by fluorescence microscopy. Positive expression appeared as red fluorescent staining with fluorescein.

Dual-modality imaging diagnosis

The myocardial HE staining results were employed as the reference standard, and a combination of myocardial segmental parameters, including SUV_{heart}, SUV_{heart}/SUV_{liver} ratio, SUV_{heart}/SUV_{lung} ration, and MCE imaging parameters (A, β, A×β, and MBFR), was used for the diagnosis of CMVD. Receiver operating characteristic (ROC) curves were constructed, and the AUC was calculated.

Statistical analysis

Data analysis was executed employing SPSS 25.0 (IBM Corp., Armonk, NY, USA). The data were succinctly summarized using the mean ± standard deviation. Single-factor ANOVA is used to compare the performance of one factor (or one treatment group) across different levels or treatment conditions. Two-factor ANOVA is used to analyze the effects of two factors (two treatment combinations) on experimental results, including whether their interaction is significant. Three-factor ANOVA is used to simultaneously analyze the effects of three factors on experimental results, including their main effects and interactions. Bonferroni analysis for multiple comparisons was used to further differentiate the groups. A P value <0.05 was considered to indicate a statistically significant difference. The relationship between the two methods was explored through Pearson correlation analysis. Reliability analysis was facilitated by employing the ICC. The AUC between models was compared using the Delong test.

Results

Basic information

The rabbits had a stable blood glucose level of 5.51±0.87 mmol/L, an ejection fraction (EF) of 74.64%±6.69%, and a shortening rate of 40.31%±5.77%.

MMI under different protocols

In the total SUV_{bw} of the heart, two-way ANOVA indicated the significant effects of pretreatment (F=43.30; P<0.001, $\eta^{2=}$0.591) and timepoint (F=10.77; P<0.001; η^2=0.152) but not for the interaction of pretreatment and timepoint (F=0.705; P=0.687; η^2=0.045). Furthermore, the simple effect of pretreatment was significant in the 30-minute examination (F=13.672; P<0.001; η^2=0.313), the 60-minute examination, (F=20.937; P<0.001; η^2=0.411), and the 90-minute examination (F=10.104; P<0.001; η^2=0.252). In the insulin group, the simple effect of timepoint was significant (F=6.715; P<0.01; η^2=0.101), while for the other four pretreatment groups, the simple effects were not significant, as illustrated in *Figure 2A*, Figures S1,S2.

For the average SUV_{bw} of liver, the main effects of pretreatment (F=4.138; P<0.01; η^2=0.121) and of timepoint (F=1.476; P<0.05; η^2=0.069) were significant, but the interaction effect between pretreatment and timepoint was not significant (F=0.059; P=1.00; η^2=0.004). Further comparisons of simple effects were made, and none of the simple effects were significant for any of the groups, as illustrated in *Figure 2B*.

For the average SUV_{bw} of the lung, the main effect of pretreatment was not significant (F=0.986; P=0.418; η^2=0.032), the main effect of timepoint was significant (F=11.192; P<0.001; η^2=0.157), and statistically significant differences were found between the 30-, 60-, and 90-minute examinations, with SUV_{lung} values becoming smaller as the examination time increased. The interaction effect between pretreatment and timepoint was not significant (F=0.07; P=1.00; η^2=0.005). In the insulin group, the simple effect of timepoint was significant (F=3.495, P=0.033, η^2=0.055), as illustrated in *Figure 2C*.

Two key parameters, the SUV_{heart}/SUV_{liver} and SUV_{heart}/SUV_{lung} ratios, were used to evaluate MMI. For the SUV_{heart}/SUV_{liver} ratio, the main effect of pretreatment was significant (F=18.84; P<0.001; η^2=0.386), but the main effect of timepoint was not significant (F=1.262; P=0.287; η^2=0.021), nor was the interaction effect between pretreatment and timepoint (F=0.303; P=0.964; η^2=0.020). For the 30-minute examination, the simple effect of pretreatment was significant (F=5.226; P<0.001; η^2=0.148); for the 60-minute examination, the simple effect of pretreatment was significant (F=9.679; P<0.001; η^2=0.244); and for the 90-minute examination, the simple effect of pretreatment was significant (F=4.538; P<0.01; η^2=0.1312) (*Figure 2D*).

For SUV_{heart}/SUV_{lung} ratio, the main effect of pretreatment was significant (F=11.784; P<0.001; η^2=0.282) as was that of timepoint (F=6.772; P<0.01; η^2=0.101), but the interaction effect between pretreatment and timepoint was not significant (F=0.450; P=0.888; η^2=0.029). For the 60-minute examination, the simple effect of pretreatment was significant (F=6.621; P<0.001; η^2=0.181), as was that for the 90-minute examination (F=4.151; P<0.01; η^2=0.122). In the insulin group, the simple effect of timepoint was significant (F=5.025; P<0.01; η^2=0.077), but the simple effects in the other four groups were not significant, as illustrated in *Figure 2E*.

Following the administration of the ^{18}F-FDG injection, the blood glucose levels in the fasted group, nonfasted group, sugar load group, acipimox group, and nonfasted-plus-insulin group were 5.98±0.45, 6.69±4.04, 8.37±0.69, 6.2±0.80, and 5.69±0.56 mmol/L, respectively. Notably, the group with a high glycemic load exhibited a significant difference in glucose levels when compared to the other four groups (P<0.01), as illustrated in *Figure 2F*; however, despite this, MMI did not yield satisfactory results, including SUV_{bw} of heart, SUV_{bw} of liver, and SUV_{bw} of lung.

For the acipimox-treated group, we closely examined the pre- and postintervention triglyceride (TG) levels,

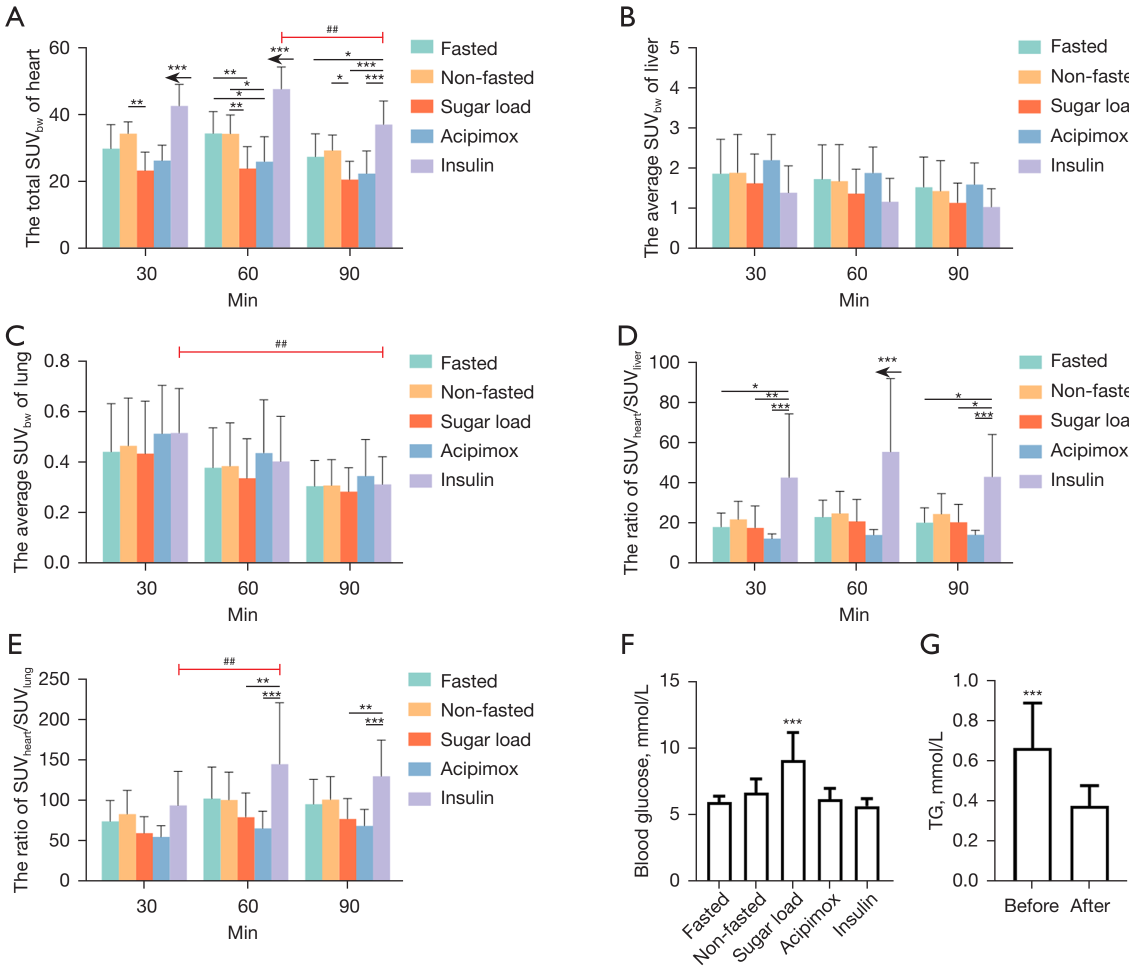

Figure 2 Analysis of the different pretreatment groups and different timepoints for MMI. (A-E) Quantitative analysis of the myocardial metabolism imaging parameters. (F) Blood glucose levels in each group at the time of injection of the FDG agent. (G) Triglyceride levels before and after acipimox administration. *, P<0.05; **, P<0.01; ***, P<0.001; ##, P<0.01. SUV_{bw}, standardized uptake value based on body weight; TG, triglyceride; FDG, fluorodeoxyglucose; MMI, myocardial metabolism imaging.

which had values of 0.69±0.22 and 0.38±0.10 mmol/L, respectively. The paired *t*-test produced a *t* score of 5.718, indicating a significant reduction in TG levels due to acipimox intervention. However, it is important to note that this intervention did not produce the desired outcomes in cardiac metabolic angiography, as shown in *Figure 2G*.

The main effects of pretreatment, timepoint, and coronary segment were all significant (P<0.001). There was an interaction between pretreatment and timepoint (P<0.05). There was an interaction between pretreatment and segment (P<0.01); however, the interaction between the three factors was not significant, as shown in *Figure 3*.

In conclusion, the nonfasted-plus-insulin group had the best image quality in the 60-minute examination, demonstrating the highest total heart uptake and the highest SUV_{heart}/SUV_{lung} ratio. Representative images are shown in *Figures 4,5*.

To confirm the robustness of our results, an interreader correlation analysis was conducted, which produced a strong ICC of 0.957 among the data assessors, as presented in *Figure 6A*.

Correlation between metabolic activity and perfusion parameters

MCE is essential for studying cardiac blood perfusion. Our

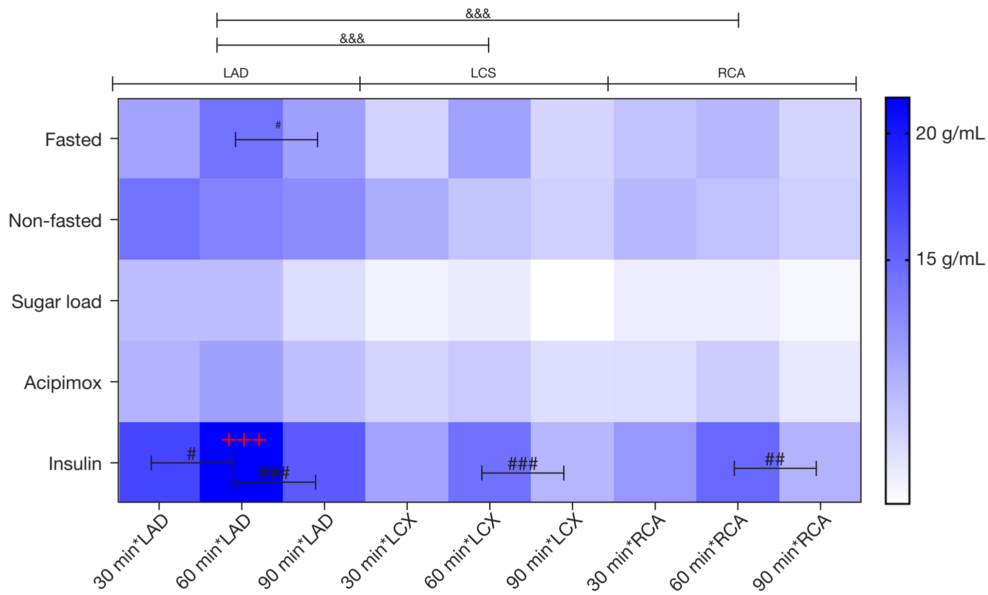

Figure 3 Three-way analysis of variance of the pretreatment conditions, timepoints, and regions of coronary blood supply. +, the same timepoint for the fasted group, nonfasted group, sugar load group, acipimox group, and nonfasted + insulin group; #, the same pretreatment group for the 30-, 60-, and 90-minute timepoints. &, the same pretreatment group for the LAD, LCX, and RCA; +++, $P<0.001$; #, $P<0.05$; ##, $P<0.01$; ###, $P<0.001$; &&&, $P<0.001$. LAD, left anterior descending artery; LCX, left circumflex artery; RCA, right coronary artery.

study collected data and images related to key parameters: blood volume (A), flow velocity (β), and resultant blood flow (MBF =A×β). Myocardial metabolic images were reconstructed using Xeleris functional imaging workstation software, including the horizontal long axis, vertical long axis, and short axis (as seen in *Figure 5B*).

These analyses were conducted within different groups as categorized by various preconditioning regimens (outlined in *Table 1*). The results showed a moderate correlation of MBFR with SUV_{bw} (r=0.686), as depicted in *Figure 6B-6F*.

A quantitative analysis model for coronary microvascular dysfunction

Based on the analysis of HE results in the 10 CMVD models, there were 44 segments in the normal group and 116 segments in the CMVD group. Both groups showed statistically significant differences in β_{rest}, β_{stress}, MBF_{rest}, MBFR, and SUV_{bw} ($P<0.05$). Meanwhile, the metabolic and perfusion measures decreased in the CMVD group (*Table 2*).

HE staining revealed the presence of inflammatory cell aggregation and mild subendocardial myocardial fibrosis in the CMVD group (*Figure 7A,7B*). In *Figure 7C*, the green arrow indicates mild myocardial fibrosis. CD31 staining showed a lower number of microvessels in the CMVD group compared to the normal group (*Figure 7D,7E*).

Both pathological histology and noninvasive imaging techniques revealed perfusion defects and a reduction of metabolic activity in the basal segment of the left ventricular septum (*Figure 7F-7I*). Representative normal and abnormal images from PET/CT MMI and MCE, along with the quantitative analysis, are shown in *Figure 7D-7O*.

ROC curve for the SUV_{bw} and MCE parameters

The ROC analysis indicated that dual diagnosis was the most effective echocardiographic predictor for identifying individuals with CMVD who would go on to develop left ventricular myocardial dysfunction (*Figure 8*). The optimal cutoff value for MBFR was 1.83, while the optimal cutoff value for SUV_{bw} was 2.42 (*Table 3*).

Discussion

The significant results obtained in this study suggest that the diagnosis of CMVD can be improved by the combined use of MMI and stress MCE imaging. Our principal results were as follows: (I) rabbits received intravenous insulin at a

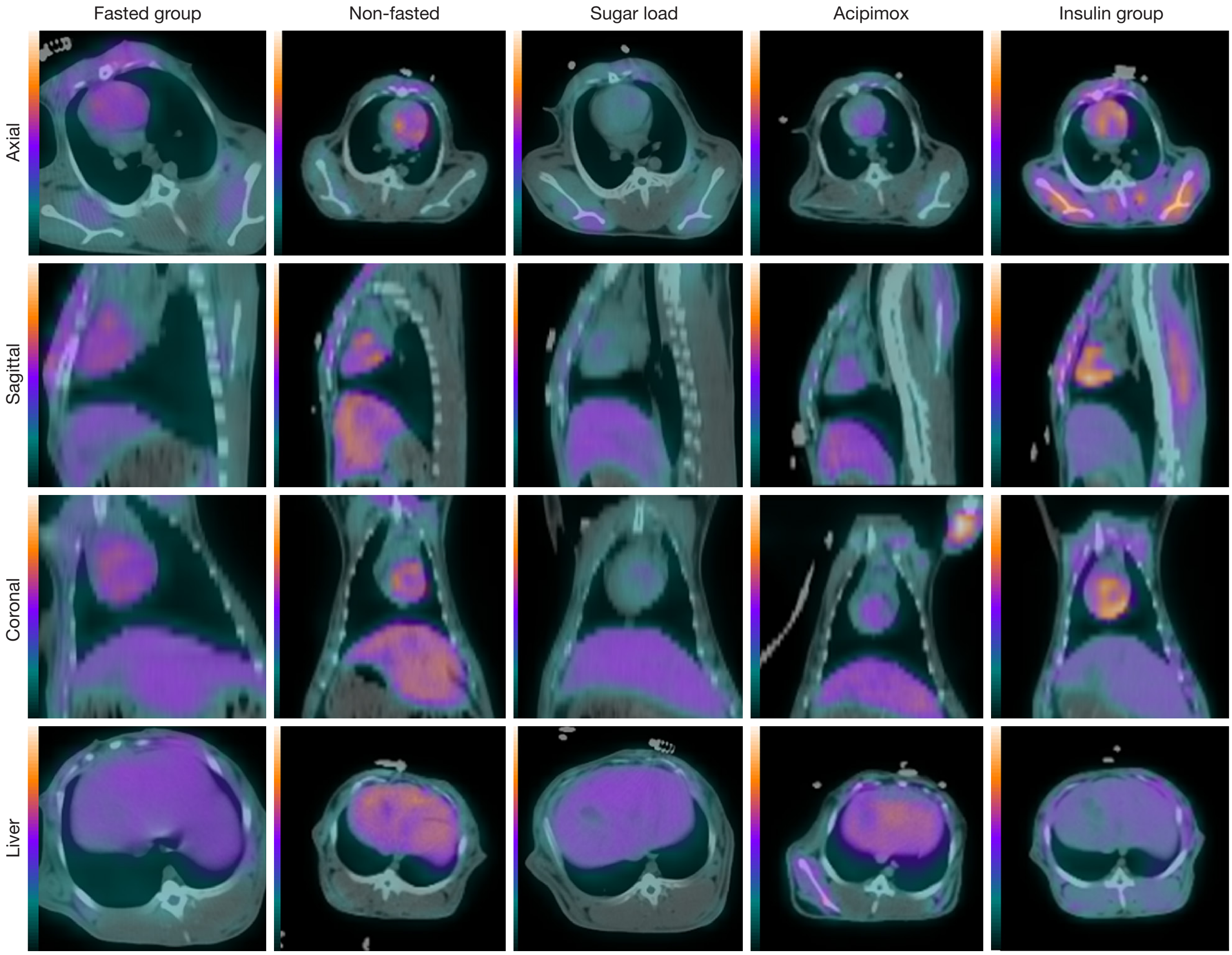

Figure 4 Myocardial metabolism images of the heart and liver in the five experimental groups. The insulin group exhibited the highest myocardial signal-to-background ratio and the lowest liver uptake.

dose of 0.1 IU/kg without dietary restrictions. Subsequently, ^{18}F-FDG was introduced under 20% hypoglycemic conditions, and precise PET scanning was performed 60 minutes after injection, resulting in high-quality ^{18}F-FDG PET images of rabbit hearts. (II) The insulin injection group exhibited a moderate correlation between SUV_{bw} and the MCE perfusion parameter of MBFR. (III) The ROC curves demonstrated that the multimodal diagnosis yield a higher prediction accuracy compared to that of the single modes.

The SUV_{bw} values in the insulin group were notably higher than those of the other groups, and this was accompanied by a decrease in hepatic uptake. The signal-to-noise ratios for the SUV_{heart}/SUV_{liver} and SUV_{heart}/SUV_{lung} ratios exhibited heightened diagnostic precision, effectively mitigating the influence of neighboring tissues, especially in the liver and lungs. Cardiomyocytes have a variety of energy sources to ensure ample energy production. Previous research has indicated that under conditions of fasting, the myocardium chiefly relies on free fatty acids as the primary energy source (13,14). However, the New Zealand White rabbit, being an herbivore with unique digestive attributes, exhibits heart and respiratory rates that are significantly higher than those of humans. Notably, conventional protocols used for enhancing myocardial metabolism imaging in humans and other animals have proven ill-suited for rabbits. The typical approach of fasting followed by glucose administration (15,16) alters the energy substrate preference of human cardiomyocytes from fatty acids to glucose, making it challenging to

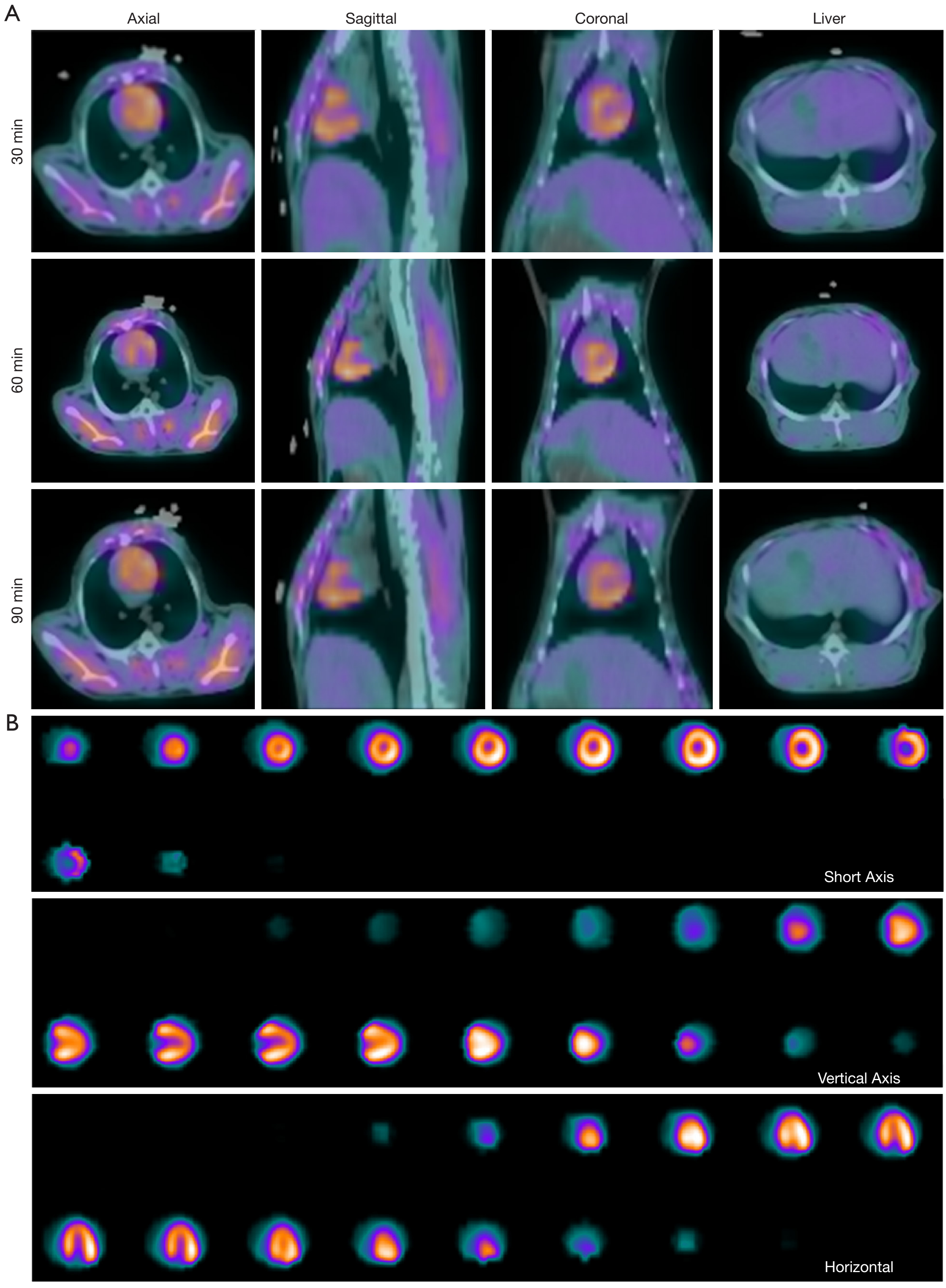

Figure 5 Myocardial metabolism images across the various scanning time windows. (A) Examinations at 60 minutes demonstrated elevated myocardial uptake and diminished liver uptake. (B) Images distinctly illustrating the uptake within each myocardial segment.

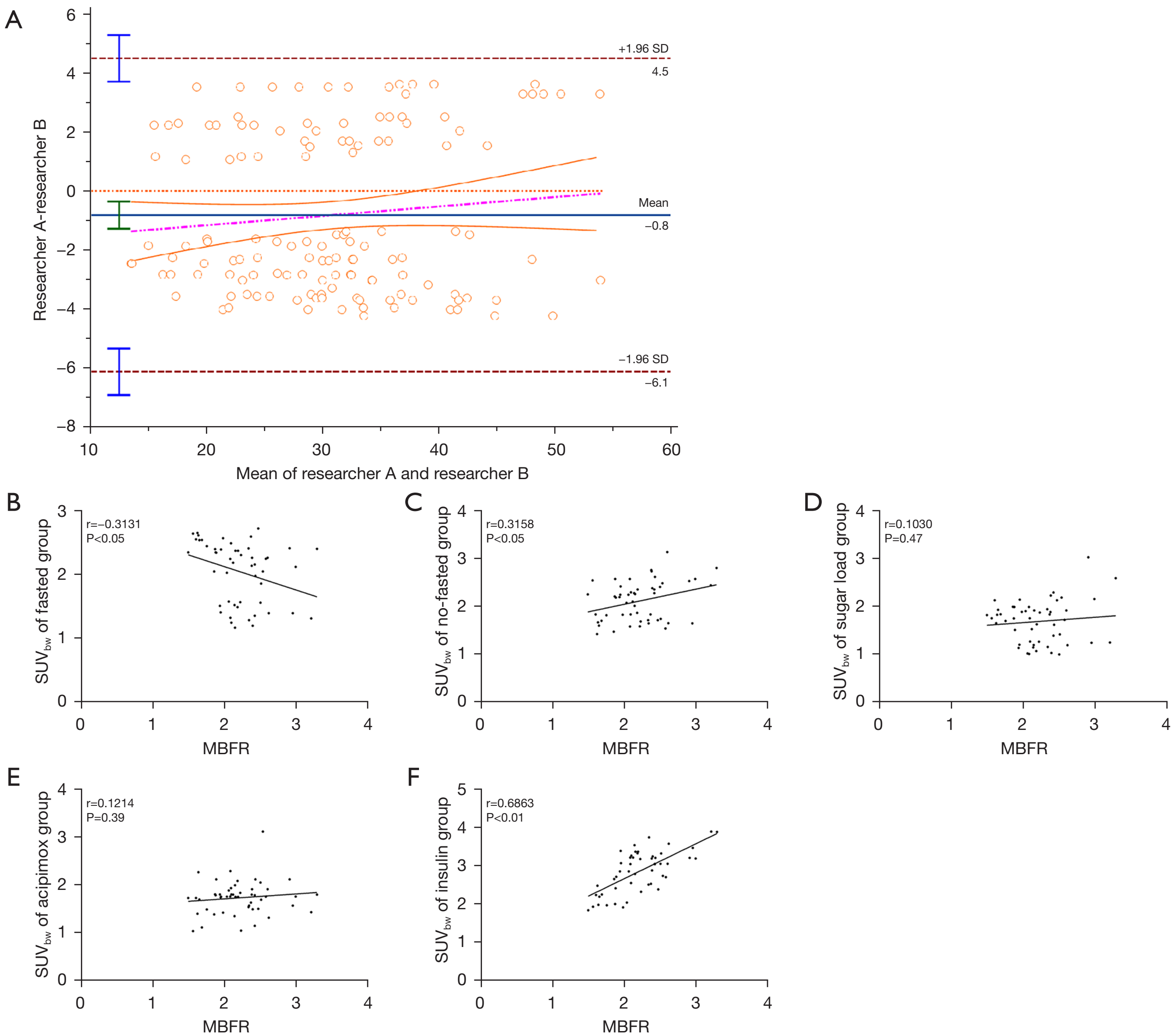

Figure 6 The correlation between myocardial SUV_{bw} uptake and MBFR in in the five groups. (A) Remarkable consensus between the two reviewers. (B-F) The correlation between myocardial SUV_{bw} uptake and MBFR was analyzed in the five groups. SD, standard deviation; MBFR, microvascular blood flow reserve; SUV_{bw}, standardized uptake value based on body weight.

Table 1 Correlation between the seven MCE parameters and myocardial SUV_{bw} in the five treatment groups

Group	β_{rest}	A_{rest}	β_{stress}	A_{stress}	MBF_{rest}	MBF_{stress}	MBFR
Fasted	−0.002	−0.038	−0.065	−0.269	−0.032	−0.301**	−0.313*
Nonfasted	0.119	−0.301*	0.389**	−0.430**	−0.093	0.131	0.316*
Sugar load	0.014	−0.142	0.174	−0.305*	−0.082	−0.042	0.103
Acipimox	0.187	−0.220	0.337*	−0.224	0.092	0.193	0.121
Nonfasted + insulin	0.115	−0.03	0.320*	−0.006	−0.162	0.394**	0.686**

*, $P<0.05$; **, $P<0.01$. MCE, myocardial contrast echocardiography; SUV_{bw}, standardized uptake value based on body weight; β, blood flow velocity; A, blood volume; MBF, myocardial blood flow; MBFR, microvascular blood flow reserve.

Table 2 Analysis of image data in the normal and CMVD groups

Parameter	Normal (n=44)	CMVD (n=116)	*t*	P
A_{rest}	2.74±1.06	2.95±1.61	–0.948	0.345
β_{rest}	9.67±1.71	10.59±2.69	–2.567	0.011*
A_{stress}	3.42±1.65	3.12±1.57	1.100	0.273
β_{stress}	11.73±3.16	10.31±3.75	2.231	0.027*
MBF_{rest}	32.87±23.96	26.59±11.17	–2.251	0.026*
MBF_{stress}	42.04±26.59	34.57±25.67	1.628	0.106
MBFR	1.70±1.02	1.14±0.62	3.371	<0.001***
SUV_{bw}	2.58±0.76	2.00±0.67	4.701	<0.001***
SUV_{heart}/SUV_{liver}	2.0±0.75	1.83±0.59	1.626	0.109
SUV_{heart}/SUV_{lung}	4.28±1.49	3.95±1.50	1.244	0.215

Data are presented as mean ± standard deviation. *, P<0.05; ***, P<0.001. CMVD, coronary microvascular disease; A, blood volume; β, blood flow velocity; MBF, myocardial blood flow; MBFR, microvascular blood flow reserve; SUV_{bw}, standardized uptake value based on body weight; SUV_{heart}, SUV of the heart; SUV_{liver}, SUV of the liver; SUV_{lung}, SUV of the lung; SUV, standardized uptake value.

pinpoint the optimal time for transition and the subsequent injection of ^{18}F-FDG. Moreover, it is essential to allow cardiomyocytes a specific duration of effective glucose metabolism. We examined how fasted and unrestricted diet influence MMI. As is widely known, fasting results in a significantly lower signal-to-background ratio (SBR), indicating cardiomyocytes reliance on fatty acids for energy and their limited glucose usage (17). Aday *et al.* (18) used acipimox for lipid reduction, while Poussier *et al.* (19) improved MMI in rats with a similar acipimox treatment. However, our study found no enhanced metabolic imaging with acipimox pretreatment. Recognizing the benefits of free feeding, we aimed to elevate rabbit plasma glucose levels using a glucose-loading regimen (20), targeting concentrations in the 7.9–8 mmol/L range. The aim of this was stimulate insulin release and create a favorable glucose gradient across cardiomyocytes. Unfortunately, these efforts did not yield the anticipated results in myocardial metabolism imaging. Thus, we concluded that rabbit blood glucose levels might not singularly dictate cardiomyocyte glucose uptake. Remarkably, by pharmacologically reducing plasma free fatty acids and TG levels using acipimox, we observed an increase in glucose utilization. To achieve this aim, enhancing the density of glucose transporter 4 on cardiomyocyte surfaces is pivotal. This hinges on boosting insulin binding to cardiomyocyte insulin receptors, thereby triggering the intracellular movement of glucose transporter 4 to the cell membrane via the PI3k pathway. This complex process amplifies glucose uptake (21-23).

This study refined the protocol for obtaining high-quality ^{18}F-FDG PET images of rabbit hearts, as it better aligns with their distinctive physiological traits. Previous literature has advised waiting at least 45 minutes after ^{18}F-FDG administration before conducting a static scan (7). In this study, due to rabbits' faster metabolism, we adapted this standard. We scanned at 30 minutes, observing early ^{18}F-FDG uptake by cardiomyocytes although blood pool activity remained. At 60 minutes, our second scan displayed optimal myocardial uptake and blood pool clearance, achieving the highest SUV_{bw} and SBR, with lower liver SUV_{bw} compared to the 30-minute scan. Over 90 minutes, myocardial SUV_{bw} declined, while liver SUV_{bw} uptake gradually decreased.

Our study links MMI with MCE outcomes, indicating the potential for a combination diagnosis for cardiac ischemia. MCE angiography is widely used for noninvasive microvascular perfusion assessment (24-26), while ^{18}F-FDG metabolism imaging can accurately reflect cardiomyocyte viability (27). Combining ^{18}F-FDG metabolism imaging and MCE is crucial for assessing myocardial vitality. Our findings included a moderate correlation between myocardial viability SUV_{bw} and perfusion reserve fraction (r=0.686). Interpreting the concordance between myocardial viability and perfusion may offer key insights (28): normal perfusion and viability may indicate a healthy myocardium, and a mismatch between perfusion and

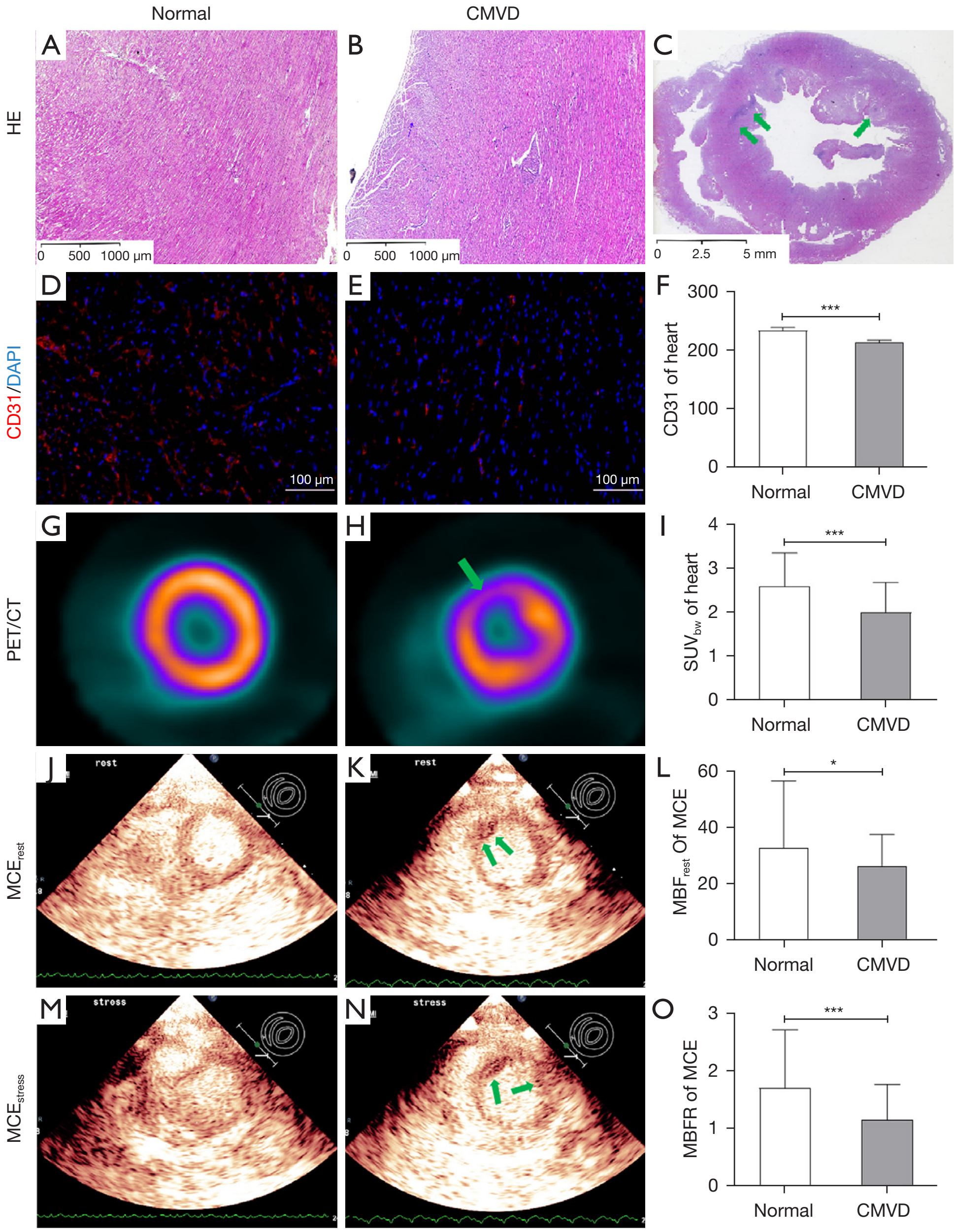

Figure 7 Pathological and imaging analyses. Normal myocardial segments are in the first column, abnormal CMVD segments are in the second column, and semiquantitative data graphs are in the third column. (A,B) Typical and atypical HE staining patterns, with blue arrow indicating subendocardial myocardial microemboli. (D,E) Microvascular analyses revealing a reduction in mean fluorescence intensity within abnormal segments. (G,H) PET/CT MMI results indicating both normal and abnormal conditions. (J,K,M,N) MCE results for both the normal and abnormal conditions depicted in (G) and (H). (C,H,K,N) Abnormal segments of the basal segment of the interventricular septum as visualized through HE staining, MCE_{rest}, MCE_{stress}, and PET/CT, with the area of defect indicated by a green arrow. (F,I,L,O) Quantitative analysis of CD31, SUV_{bw}, MBF, and MBFR. (A,B) HE staining of myocardial tissue (original magnification 20×). (C) HE staining of myocardial tissue (original magnification 0.44×). (D,E) Immunofluorescence staining of myocardial tissue with CD31 (original magnification 20×). *, P<0.05; ***, P<0.001. CMVD, coronary microvascular disease; DAPI, 4',6-diamidino-2-phenylindole; PET/CT, positron emission tomography/computed tomography; SUV_{bw}, standardized uptake value based on body weight; MCE, myocardial contrast echocardiography; MBF, myocardial blood flow; MBFR, microvascular blood flow reserve; HE, hematoxylin and eosin; MMI, myocardial metabolism imaging.

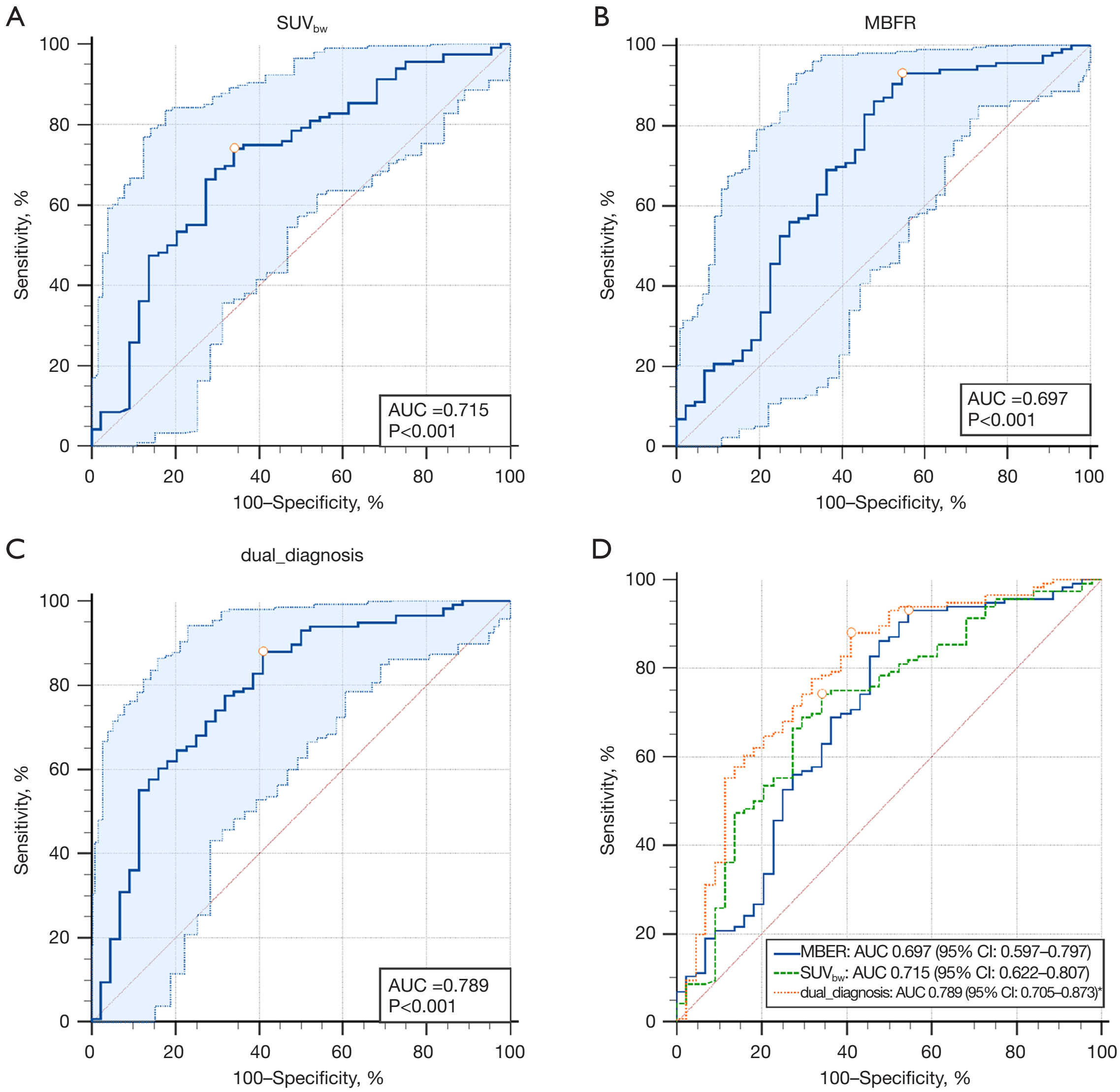

Figure 8 ROC curve of the diagnostic accuracy of SUV_{bw}, MBFR, and the combined diagnosis. Notably, the ROC curve representing combined diagnosis exhibited the highest AUC value. *, P<0.05. SUV_{bw}, standardized uptake value based on body weight; AUC, area under the curve; MBFR, microvascular blood flow reserve; ROC, receiver operating characteristic.

Table 3 The ROC curve of CMVD diagnosis

Parameter	AUC (95% CI)	Sensitivity% (95% CI)	Specificity% (95% CI)	+LR	−LR	Youden index J	Cutoff
MBFR	0.697 (0.597–0.797)	93.1 (86.9–97.0)	45.45 (30.4–61.2)	1.71	0.15	0.3856	≤1.83
SUV_{bw}	0.715 (0.622–0.807)	74.14 (65.2–81.8)	65.91 (50.1–79.5)	2.17	0.39	0.4005	≤2.42
Combined diagnosis	0.789* (0.705–0.873)	87.93 (80.6–93.2)	59.09 (43.2–73.7)	2.15	0.20	0.4702	–

AUC: 0.5–0.7, low accuracy; 0.7–0.9, moderate accuracy; >0.9, high accuracy. *, P<0.05. ROC, receiver operating characteristic; CMVD, coronary microvascular disease; AUC, area under the curve; CI, confidence interval; +LR, positive likelihood ratio; −LR, negative likelihood ratio; MBFR, microvascular blood flow reserve; SUV_{bw}, standardized uptake value based on body weight.

metabolism (increased perfusion, reduced ^{18}F-FDG uptake in defects) may indicate viable ischemic tissue. Common agents for perfusion imaging, such as $^{13}N\text{-}NH_3$, ^{201}TI, are challenging to prepare and use. In contrast, MCE, being radiation free and easily applied, suits myocardial blood perfusion evaluation. Reant *et al.* (29) reported that an MCE method for a diagnosing for coronary stenosis had an AUC value of 0.66, which aligns with the findings of our study. Furthermore, we identified a cutoff value of <1.83 for MBFR in diagnosing CMVD. In Lautamäki *et al.*'s (30) study on myocardial microcirculation postinfarction in pigs, FDG PET/CT yielded a diagnostic rate of 0.68, which is consistent with our study, in which we used a corresponding cutoff value for SUV_{bw} of <2.42 in CMVD diagnosis. Notably, we observed a significant improvement in CMVD diagnosis through the combined assessment of SUV_{bw} and MBFR.

Overall, our study highlights the viability of using a simple premedication approach with free feeding and intravenous insulin to produce high-quality gated heart FDG-PET images in adult New Zealand white rabbits. The achieved signal-to-noise ratio rivals that observed for humans. This insulin-augmented PET technique holds great application potential for ischemic heart disease research involving rabbits. Comprehensive analysis of myocardial metabolism and perfusion levels improves the diagnosis of CMVD disease.

In addition to the inherent limitations of using animal models for studying human diseases, our research has its own specific constraints. The first is the relatively small sample size. The second is the cost of small-animal PET/CT imaging and the clinical equipment used in this experiment. In future studies, we are committed to achieving the precise diagnosis of CMVD at the molecular imaging level.

Conclusions

This study demonstrated the feasibility of a simple premedication approach using free feeding and intravenous insulin, which produced high-quality gated heart ^{18}FDG PET/CT images in adult male New Zealand white rabbits. This technique may be productively applied in ischemic heart disease research in rabbits and may improve CMVD diagnosis through the comprehensive assessment of myocardial metabolism and perfusion.

Acknowledgments

This work was supported by the Xinjiang Key Laboratory of Ultrasound Medicine and the Department of Nuclear Medicine at The First Affiliated Hospital of Xinjiang Medical University.

Funding: This research was supported by the Natural Science Foundation of China (grant No. 32071459).

Footnote

Reporting Checklist: The authors have completed the ARRIVE reporting checklist. Available at https://qims.amegroups.com/article/view/10.21037/qims-23-1630/rc

Conflicts of Interest: All authors have completed the ICMJE uniform disclosure form (available at https://qims.amegroups.com/article/view/10.21037/qims-23-1630/coif). The authors have no conflicts of interest to declare.

Ethical Statement: The authors are accountable for all aspects of the work in ensuring that questions related to the accuracy or integrity of any part of the work are appropriately investigated and resolved. Experiments were performed under a project license (No. IACUC-20210725-15) granted by the Experimental Animal Ethics Committee of Xinjiang Medical University and in compliance with institutional guidelines for the care and use of animals.

References

1. Roth GA, Mensah GA, Fuster V. The Global Burden of Cardiovascular Diseases and Risks: A Compass for Global Action. J Am Coll Cardiol 2020;76:2980-1.
2. Crea F, Montone RA. Pathophysiology of coronary

microvascular dysfunction. Vascul Pharmacol 2023;153:107239.
3. Tonet E, Pompei G, Faragasso E, Cossu A, Pavasini R, Passarini G, Tebaldi M, Campo G. Coronary Microvascular Dysfunction: PET, CMR and CT Assessment. J Clin Med 2021;10:1848.
4. Schindler TH, Dilsizian V. Coronary Microvascular Dysfunction: Clinical Considerations and Noninvasive Diagnosis. JACC Cardiovasc Imaging 2020;13:140-55.
5. Almeida AG, Carpenter JP, Cameli M, Donal E, Dweck MR, Flachskampf FA, Maceira AM, Muraru D, Neglia D, Pasquet A, Plein S, Gerber BL; Reviewers: This document was reviewed by members of the 2018–2020 EACVI Scientific Documents Committee; chair of the 2018–2020 EACVI Scientific Documents Committee; 2018–2020 EACVI President: Multimodality imaging of myocardial viability: an expert consensus document from the European Association of Cardiovascular Imaging (EACVI). Eur Heart J Cardiovasc Imaging 2021;22:e97-e125.
6. Bansal A, Ananthasubramaniam K. Cardiovascular positron emission tomography: established and emerging role in cardiovascular diseases. Heart Fail Rev 2023;28:387-405.
7. Dilsizian V, Bacharach SL, Beanlands RS, Bergmann SR, Delbeke D, Dorbala S, Gropler RJ, Knuuti J, Schelbert HR, Travin MI. ASNC imaging guidelines/SNMMI procedure standard for positron emission tomography (PET) nuclear cardiology procedures. J Nucl Cardiol 2016;23:1187-226.
8. Capdeville S, Gholson BA, Lindner JR. Contrast Echocardiography for Assessing Myocardial Perfusion. Curr Cardiol Rep 2023;25:1581-7.
9. Evangelou D, Bechlioulis A, Tzeltzes G, Lakkas L, Theodorou I, Kalaitzidis R, Dounousi E, Michalis LK, Naka KK. Myocardial strain indices and coronary flow reserve are only mildly affected in healthy hypertensive patients. Int J Cardiovasc Imaging 2021;37:69-79.
10. Mehta PK, Huang J, Levit RD, Malas W, Waheed N, Bairey Merz CN. Ischemia and no obstructive coronary arteries (INOCA): A narrative review. Atherosclerosis 2022;363:8-21.
11. Jeong J, Kong E, Chun K, Cho I. The Impact of Energy Substrates, Hormone Level and Subject-Related Factors on Physiologic Myocardial (18)F-FDG Uptake in Normal Humans. Nucl Med Mol Imaging 2013;47:225-31.
12. Feng Y, Bogaert J, Oyen R, Ni Y. An overview on development and application of an experimental platform for quantitative cardiac imaging research in rabbit models of myocardial infarction. Quant Imaging Med Surg 2014;4:358-75.
13. Ritterhoff J, Tian R. Metabolism in cardiomyopathy: every substrate matters. Cardiovasc Res 2017;113:411-21.
14. Fillmore N, Mori J, Lopaschuk GD. Mitochondrial fatty acid oxidation alterations in heart failure, ischaemic heart disease and diabetic cardiomyopathy. Br J Pharmacol 2014;171:2080-90.
15. Mhlanga J, Derenoncourt P, Haq A, Bhandiwad A, Laforest R, Siegel BA, Dehdashti F, Gropler RJ, Schindler TH. 18F-FDG PET in Myocardial Viability Assessment: A Practical and Time-Efficient Protocol. J Nucl Med 2022;63:602-8.
16. Julien HM, DeLuca A, Lin J, Bokhari S. Reduced dose oral glucose load yields excellent myocardial pet viability images. Journal of the American College of Cardiology 2017;69:1523.
17. Ahmadpour S, Habibi MA, Hosseinimehr SJ. Various Aspects of Fasting on the Biodistribution of Radiopharmaceuticals. Curr Drug Metab 2022;23:827-41.
18. Aday AW, Goldfine AB, Gregory JM, Beckman JA. Impact of Acipimox Therapy on Free Fatty Acid Efflux and Endothelial Function in the Metabolic Syndrome: A Randomized Trial. Obesity (Silver Spring) 2019;27:1812-9.
19. Poussier S, Maskali F, Tran N, Person C, Maureira P, Boutley H, Karcher G, Lacolley P, Régnault V, Fay R, Marie PY. ECG-triggered 18F-fluorodeoxyglucose positron emission tomography imaging of the rat heart is dramatically enhanced by acipimox. Eur J Nucl Med Mol Imaging 2010;37:1745-50.
20. Dilsizian V, Bacharach SL, Beanlands RS, Bergmann SR, Delbeke D, Gropler RJ. ASNC imaging guidelines for nuclear cardiology procedures: PET myocardial perfusion and metabolism clinical imaging. J Nucl Cardiol 2009;16:651.
21. Sun XX, Li S, Wang Y, Li W, Wei H, He ZX. Rescue Protocol to Improve the Image Quality of 18F-FDG PET/CT Myocardial Metabolic Imaging. Clin Nucl Med 2021;46:369-74.
22. Zhou Q, Sun WW, Chen JC, Zhang HL, Liu J, Lin Y, Lin PC, Wu BX, An YP, Huang L, Sun WX, Zhou XW, Li YM, Yuan YY, Zhao JY, Xu W, Zhao SM. Phenylalanine impairs insulin signaling and inhibits glucose uptake through modification of IRβ. Nat Commun 2022;13:4291.
23. Zhao H, Lu J, He F, Wang M, Yan Y, Chen B, Xie D, Xu C, Wang Q, Liu W, Yu W, Xi Y, Yu L, Yamamoto T, Koyama H, Wang W, Zhang C, Cheng J. Hyperuricemia contributes to glucose intolerance of hepatic inflammatory macrophages and impairs the insulin signaling pathway

via IRS2-proteasome degradation. Front Immunol 2022;13:931087.
24. Roldan P, Masri A, Hodovan J, Lindner J. Vasodilator stress myocardial contrast echocardiography detects abnormal myocardial microvascular perfusion in patients with hypertrophic cardiomyopathy. JACC 2021;77:1385.
25. Liu J, Wang Y, Zhang J, Li X, Tan L, Huang H, Dai Y, Shang Y, Shen Y. Dynamic evolution of left ventricular strain and microvascular perfusion assessed by speckle tracking echocardiography and myocardial contrast echocardiography in diabetic rats: Effect of dapagliflozin. Front Cardiovasc Med 2023;10:1109946.
26. Zhang J, Li X, Liu J, Shang Y, Tan L, Guo Y. Early and dynamic detection of doxorubicin induced cardiotoxicity by myocardial contrast echocardiography combined with two-dimensional speckle tracking echocardiography in rats. Front Cardiovasc Med 2022;9:1063499.
27. Wang F, Xu W, Lv W, Du D, Feng H, Zhang X, Wang S, Chen W, Lu L. Evaluation of the diagnostic value of joint PET myocardial perfusion and metabolic imaging for vascular stenosis in patients with obstructive coronary artery disease. J Nucl Cardiol 2021;28:3070-80.
28. Nakajima K, Wakabayashi H. Value of combined perfusion and metabolic tracers versus stress-rest perfusion imaging for coronary heart disease. J Nucl Cardiol 2021;28:3081-4.
29. Reant P, Labrousse L, Lafitte S, Tariosse L, Bonoron-Adele S, Padois P, Roudaut R, Dos Santos P, DeMaria A. Quantitative analysis of function and perfusion during dobutamine stress in the detection of coronary stenoses: two-dimensional strain and contrast echocardiography investigations. J Am Soc Echocardiogr 2010;23:95-103.
30. Lautamäki R, Schuleri KH, Sasano T, Javadi MS, Youssef A, Merrill J, Nekolla SG, Abraham MR, Lardo AC, Bengel FM. Integration of infarct size, tissue perfusion, and metabolism by hybrid cardiac positron emission tomography/computed tomography: evaluation in a porcine model of myocardial infarction. Circ Cardiovasc Imaging 2009;2:299-305.

Cite this article as: Wang G, Li X, Zhao J, Chen S, Qin Y, Guan L, Mu Y. Integrating myocardial metabolic imaging and stress myocardial contrast echocardiography to improve the diagnosis of coronary microvascular diseases in rabbits. Quant Imaging Med Surg 2024;14(8):5915-5931. doi: 10.21037/qims-23-1630

